Formation and variability of the South Pacific Sea Surface Salinity maximum in recent decades

Audrey Hasson, Thierry Delcroix, Jacqueline Boutin

JOURNAL OF GEOPHYSICAL RESEARCH: OCEANS, VOL. 118, 5109–5116, doi:10.1002/jgrc.20367, 2013

Formation and variability of the South Pacific Sea Surface Salinity maximum in recent decades

Audrey Hasson,[1] Thierry Delcroix,[1] and Jacqueline Boutin[2]

Received 13 June 2013; revised 19 August 2013; accepted 20 August 2013; published 8 October 2013.

[1] This study investigates causes for the formation and variability of the Sea Surface Salinity maximum (SSS > 36) centered near 18°S–124°W in the South Pacific Ocean over the 1990–2011 period at the seasonal time scale and above. We use two monthly gridded products of SSS based on in situ measurements, high-resolution along-track Voluntary Observing Ships thermo-salinograph data, new SMOS satellite data, and a validated ocean general circulation model with no direct SSS relaxation. All products reveal a seasonal cycle of the location of the 36-isohaline barycenter of about ±400 km in longitude in response to changes in the South Pacific Convergence Zone location and Easterly winds intensity. They also show a low frequency westward shift of the barycenter of 1400 km from the mid 1990s to the early 2010s that could not be linked to the El Nino Southern Oscillation phenomena. In the model, the processes maintaining the 22 year equilibrium of the high salinity in the mixed layer are the surface forcing (∼+0.73 pss/yr), the horizontal salinity advection (∼−0.37 pss/yr), and processes occurring at the mixed layer base (∼−0.35 pss/yr).

Citation: Hasson, A., T. Delcroix, and J. Boutin (2013), Formation and variability of the South Pacific Sea Surface Salinity maximum in recent decades, *J. Geophys. Res. Oceans*, *118*, 5109–5116, doi:10.1002/jgrc.20367.

1. Introduction

[2] The global distribution of mean Sea Surface Salinity (SSS) shows the existence of one large-scale high-salinity core centered within about 15–30° latitude in each hemisphere of the Atlantic and Pacific oceans [e.g., *Levitus*, 1986]. Analyses of observations and model outputs have indicated that these cores mainly owe their existence to the positive evaporation minus precipitation ($E-P$) budget and wind-driven Ekman salt transport, the latter accounting for the 5–10° latitude poleward shift of the SSS maxima relative to the $E-P$ maxima [e.g., *Delcroix and Henin*, 1991; *Foltz and McPhaden*, 2008; *Qu et al*., 2011].

[3] The climatic relevance of these high-salinity cores has been discussed in many articles. At seasonal to decadal time scales, salinity (and so density) changes in these cores affect the source branches of shallow tropical-subtropical overturning cells (STCs) and the generation of spiciness anomalies [*McCreary and Lu*, 1994; *Gu and Philander*, 1997; *O'Connor et al*., 2002; *Nonaka and Sasaki*, 2007; *Kolodziejczyk and Gaillard*, 2012]. These, in turn, are thought to influence the mean background temperature distribution in the equatorial band and hence could modulate low-frequency tropical variability [*Schneider et al*., 1999; *McPhaden and Zhang*, 2004; *Laurian et al*., 2009]. At the multidecadal time scale, the observations of positive salinity trends in these cores have been interpreted as the likely signature of global change [*Cravatte et al*., 2009; *Durack and Wijffels*, 2010; *Terray et al*., 2012]. To the first order, these trends result from the $E-P$ forcing increase in positive $E-P$ regions as expected by the Clausius Clapeyron relationship in a warming world [*Held and Soden*, 2006; *Seager et al*., 2010]. Recent model studies further suggest that not only the amplitude but also the location of the maximum $E-P$ forcing may change in the future climate in response to global warming [*Seager et al*., 2010; *Scheff and Frierson*, 2012]. It is thus crucial to monitor SSS changes in these cores in order to better understand their relationship to climate change. Besides, these large spatial areas of rather constant SSS with different SST, wind stress, and $E-P$ conditions are ideal for the calibration and the validation of SSS estimates from SMOS and Aquarius satellites.

[4] Studies of high-salinity cores have so far mostly focused on the northern hemisphere structures. Little work has been done for the southern hemisphere, mostly due to the lack of sufficient observations. The goal of this paper is, therefore, to analyze causes for the formation and variability of the poorly documented south Pacific high-salinity core, relying on multidecadal in situ SSS data collection, recent SMOS-derived measurements, and a validated OGCM simulation. As shown in Figure 1a, the mean core stretches as an ellipse-type surface in the eastern half of the south tropical Pacific around 25°S–10°S and

[1]LEGOS, UMR 5566, CNES, CNRS, IRD, Université de Toulouse, Toulouse, France.
[2]LOCEAN/IPSL, UMR 7159, CNRS-INSU, UPMC, IRD, MNHN, Paris, France.

Corresponding author: A. Hasson, LEGOS, UMR 5566, CNES, CNRS, IRD, Université de Toulouse, 14 avenue Edouard Belin, 31400 Toulouse CEDEX, France. (Audrey.Hasson@legos.obs-mip.fr)

2169-9275/13/10.1002/jgrc.20367

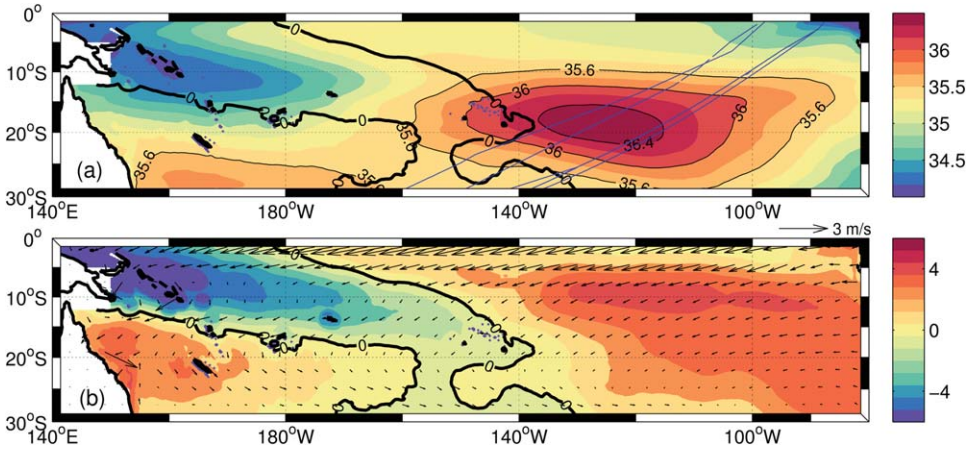

Figure 1. (a) Mean 1990–2011 modeled mixed-layer salinity (MLS). The blue lines represent the Matisse Ship routes of 2010 and 2011 discussed in the main text. (b) Mean evaporation−precipitation ($E-P$) based on ERAi; units are mm/day. Overplotted as arrows are the mean modeled surface currents. The 0 isohyet is shown on both panels with a bold black solid line.

150°W–100°W. The SSS values are always higher than 36 pss over a mean surface of 5.2×10^6 km^2, that is, about 2/3 of the Australian continent size.

[5] The paper is organized as follows. Section 2 describes the in situ, SMOS, and model-derived SSS, and compares these complementary SSS products; section 3 focuses on causes of the core formation looking at its mean salinity budget; and section 4 analyzes its seasonal and interannual variability and "long-term" trend. Summary and conclusion appear in section 5.

2. Data Description and Assessment

[6] We use the Pacific Ocean gridded SSS product from *Delcroix et al*. [2011] which is available monthly on a 1° longitude by 1° latitude spatial grid, within the 30°N–30°S, 120°E–70°W domain from 1950 to 2008. This product, recently extended to 2009, is an objective analysis of in situ observations collected within 0–10 m from Voluntary Observing Ships (VOS), TAO/TRITON moorings, Argo buoys, and CTD casts. Following *Hasson et al*. [2013, hereafter HDD13], only gridded values with normalized errors <0.7 will be considered, restricting our confidence to values located in the western half of the high-salinity core before the Argo era (see HDD13). As a complement, especially for studying the recent interannual changes, we also use a monthly, ½° by ½° global (77°S–66.5°N) gridded SSS product. The SSS values are then derived from an objective analysis of Argo data using the in situ analysis system (ISAS, 6th version) tool not including VOS measurements [see *Gaillard et al*., 2009]. This product covers the 2002–2012 years, but only data with an associated error below 80% were kept. Consequently, most data from 2002 to 2003 are discarded because of the poor data coverage in our studied region. Argo data between 0 and 10 m were averaged to represent SSS.

[7] We also use the original high-resolution along-track in situ SSS data collected from VOS crossing the high-salinity core along two different routes during their southward and northward voyages between Europe and New Zealand via the Panama channel (see Figure 1a, blue lines). The French SSS Observation Service has instaled thermosalinographs (TSGs) on VOS as early as 1992. Median SSS values assumed to represent 0–10 m are recorded every 5 min (i.e., every 3 km at 20 knots) from prescribed 15 s sample rate [*Henin and Grelet*, 1996]. The data quality was estimated from different tests involving comparison with climatology, daily bucket samples collected on board and collocated near-surface Argo data. Only "Good" and "Probably Good" flagged data were kept for our study.

[8] We further use the outputs of an OGCM ran by the DRAKKAR group using the NEMO *z*-coordinate model [*Madec*, 2008] in its version 3.2.1. The model configuration (ORCA025.L75-MRD911) has been presented in details by HDD13. The run was extended by 2 years and now covers the 1990–2011 period. The simulation was forced by a globally corrected ERA-interim reanalysis to prevent direct SSS restoring. Each term of the salt conservation equation (see equation (1) below) was computed at each simulation time step (960 s). The simulation output is archived every 5 days, on its original global 0.25° latitude by 0.25° longitude grid mesh with 75 vertical levels. Salinity values within the upper 9.8 m were averaged to represent SSS.

[9] SMOS satellite was launched in November 2009 and retrieved SSS data are available from January 2010 to present. We use the ESA level 2 data (v5 reprocessing) weighted averages produced by the LOCEAN team in Paris as described in *Boutin et al*. [2013]. It does not include strong relaxation to the climatology and thus preserves interannual variability [*Reul et al*., 2013]. SSS maps are made of SSS (assumed to represent the 0–10 cm) averaged over 10 days or 1 month and over 1° × 1° and are oversampled on a 0.25° latitude by 0.25° longitude grid. As noted above, high-salinity core regions are ideal for satellite SSS retrieval as SST is warm (above 20°C), wind is moderate, and in the particular case of the South Pacific Ocean, the core is also far from the land and far from Radio Frequency Interferences sources. In addition, in the SMOS/ESA processing, a large part of the south-east Pacific region (45°S–5°S–95°W–140°W) are taken as a reference for calibrating SMOS data every 2 weeks, thus optimizing seasonal biases correction in our region.

[10] The model outputs are routinely evaluated by the DRAKKAR team against various metrics, and it was further carefully evaluated within the tropical Pacific Ocean (30°N–30°S) in HDD13. The model outputs were compared to the 1950–2009 gridded SSS products as described above and to the TAO-TRITON near-surface currents. The assessment showed, in particular, a good representation of the mean, seasonal, and interannual (ENSO) variability in SSS. HDD13 further underlined the model ability to quantify all terms of the mixed-layer salinity (MLS) budget that can only be qualitatively computed or inferred as a residual from observations.

[11] *Boutin et al*. [2013] evaluated SMOS SSS against the ISAS product in various regions of the global ocean with 5 day and 50 km colocation radius. In the northern subtropical Atlantic salinity maximum, they found a standard deviation of the difference of 0.28 and a mean bias of −0.13. In this study, we extend the colocation radius to 9 days, in order to cover the 18 day SMOS repeat subcycle. For the same region, this reduces the standard deviation of the differences by 18%.

[12] The model and SMOS ability to reproduce small-scale in situ SSS were assessed for our studied region using eight high-resolution VOS TSG transects. A representative example of a voyage across the high SSS core in February 2011 is shown in Figure 2. For a collocation radius of 9 days and 50 km (and averaging the along-track in situ SSS data over 20–30 km, i.e., close to the model and SMOS grid sizes), the standard deviations of the differences between SMOS and in situ SSS and modeled SSS and in situ SSS are 0.20 and 0.26, and the mean biases are −0.08 and 0.07, respectively (statistics computed over 1502 data points).

[13] Having gained reasonable confidence in the model and SMOS data, the remaining part of this paper relies mostly on the model outputs enabling us to properly quantify terms of the salinity budget; whenever available, the gridded in situ and/or SMOS SSS data will be used to reinforce our conclusions.

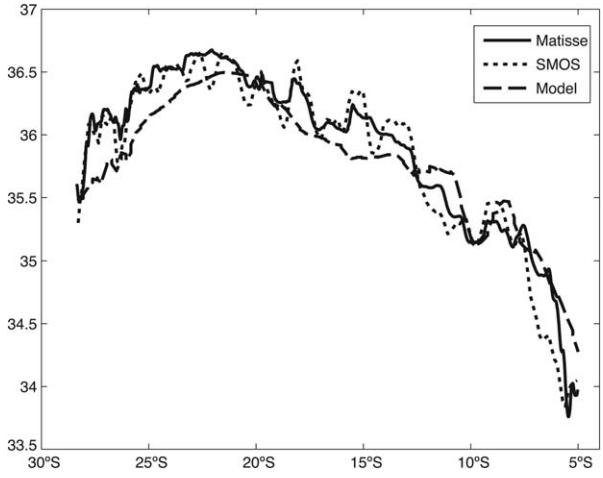

Figure 2. Comparison between near-surface salinity data derived from (black line) the TSG instrument instaled on board M/V Matisse and the collocated SSS: (dashed line) modeled and (dotted line) SMOS values. The Matisse salinity values were obtained during 20–27 February 2011 along the northern shipping line shown in Figure 1a.

3. Causes of the High-Salinity Core Formation

[14] The mean modeled SSS, surface current, and $E-P$ forcing fields for the south tropical Pacific are shown in Figure 1 to set the context. (See Figure 1a from HDD13 for an analogous observed SSS map.) As stated above, there is a clear southwest shift between the location of the SSS maxima (SSS > 36 pss) and the $E-P$ maxima (>2 mm/day), consistent with the mean surface current direction. Not shown here, the location of mean $E-P$ maxima coincides with the location of maximum wind speed that governs the strength of E process. To quantify causes of the high-salinity core formation, we looked at the MLS budget. Following HDD13, the MLS balance may be written as

$$\underbrace{\partial_t\langle S\rangle}_{I} = \underbrace{\frac{(E-P)}{H}.\langle S\rangle}_{II} - \underbrace{\langle \vec{u}_h\cdot\vec{\nabla}_h S\rangle}_{III} + \underbrace{\frac{(w_e+d_tH)\cdot\delta S}{H}}_{IV} + \underbrace{\left\langle \vec{\nabla}_h\left(K_h\cdot\vec{\nabla}_h S\right)\right\rangle}_{V} + \underbrace{\frac{\partial_z(K_z\cdot\delta S)}{H}}_{VI} \quad (1)$$

where $\langle X\rangle = \frac{1}{H}\int_{-H}^{0} X(z)dz$, S denotes salinity within the mixed layer of depth H, $(E-P)$ the evaporation and precipitation difference (defined positive out of the ocean), u_h is the horizontal velocity vector averaged within the mixed layer (having (u) and (v) components defined as positive eastward (x) and northward (y), respectively), w_e is the entrainment velocity at the base of the mixed layer, δS is the salinity jump at the base of the mixed layer, and K_h and K_v are the horizontal and vertical diffusion coefficients, respectively. We consider influence of river runoffs as negligible in the southeast tropical Pacific. The term (I) in equation (1) is referred to as the MLS tendency, term (II) as the surface forcing, terms (III) and (V) together as the horizontal advection, and terms (IV) and (VI) together as the subsurface forcing.

[15] Figure 3 shows the 1990–2011 averaged contributions of the surface and subsurface forcing and horizontal advection terms for high-salinity regions delimited by three different isohalines, where SSS is 36.0 pss or saltier, the 1990–2011 MLS tendency is +0.02 pss/yr (not shown). The surface forcing is the dominant (positive) term removing fresh water from the ocean, with a mean contribution of about +0.73 pss/yr. On average, the off-line calculation based on the model output suggests that E and P, respectively, account for about +4/3 and −1/3 of the surface forcing term. Horizontal advection makes a negative contribution to the salt budget, bringing low-salinity waters from the northeast (see Figure 1a), with a mean contribution of −0.36 pss/yr (i.e., −0.08, −0.15, and −0.12 pss/yr for zonal and meridional advections (term III) and horizontal diffusion (term V), respectively). About half of the

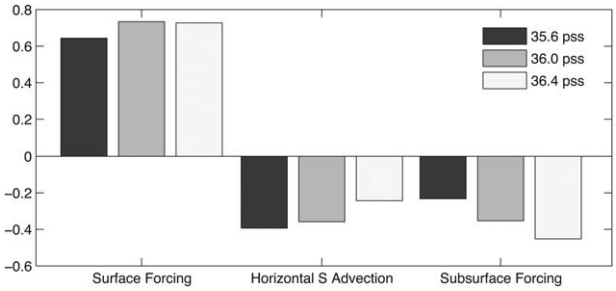

Figure 3. Mean modeled mixed-layer salinity budgets (pss/yr) in the high-salinity regions bounded by the 35.6, 36, and 36.4 isohalines shown in Figure 1a.

surface forcing is thus balanced by horizontal advection, the other half (−0.35 pss/yr) being due to the subsurface forcing, by mixing high-salinity waters with waters below the near-surface layer. Figure 3 also quantifies the mean salinity budget in regions delimited by the 35.6 and 36.4 isohalines. Overall, the surface forcing remains rather constant for any chosen high-salinity regions, while the horizontal advection decreases and the subsurface forcing increases as the isohalines grow. This is due to a reduction of the horizontal salinity gradients and to an increase of the vertical salinity gradients (not shown here) from the 35.6 to the 36.4 pss and saltier regions.

4. Variability of the High-Salinity Core

4.1. Seasonal Variability

[16] To analyze the seasonal variability of the high-salinity region, we constructed an MLS mean monthly year from both the 1990–2011 modeled and the 1990–2009 observed data, and for each of the terms in equation (1). The monthly climatologies were calculated after filtering out the possible influence of interannual (ENSO) changes, as detailed in HDD13. As only 2 years (2010–2011) of data were available for SMOS, the corresponding mean year in MLS was constructed without filtering.

[17] The modeled high-salinity region (SSS > 36 pss) shows virtually no seasonal variability in its absolute maximum SSS values and size (not shown) but does in its location as indicated by the horizontal displacements of the monthly 36 isohaline contours in Figure 4a. The 36 isohaline extends as far as 155°W to the west during austral summer and 100°W to the east in winter with weak meridional displacement. The mean 36-isohaline barycenter is located at 18.4°S–123.8°W. It reaches its easternmost position in March (120.3°W) and westernmost position in September (127.7°W), driving a zonal cycle with around 400 km amplitude (see the colored dots in Figure 4a and black dots in Figure 5a). The seasonal meridional cycle of the barycenter is relatively negligible. The SMOS-derived zonal barycenter cycle (stars in Figure 5a) is close to being in temporal phase with the modeled one. There are, however, a couple of degrees of latitude shift possibly reflecting issues in SMOS SSS retrieval and/or the different considered time periods and ENSO filtering. The same comparison cannot be directly applied to *Delcroix et al*. [2011] gridded SSS product as the eastern half of the high-salinity region lacks of in situ data and thus, holds a mean normalized error above 0.7 (see HDD13). As an alternative, the barycenter displacement was compared for data west of 120°W only from both the model and the gridded product (gray dots and diamonds in Figure 5a). Again, the observed and modeled barycenter seasonal displacements do agree. Hence, observations both from SMOS and the gridded product show seasonal zonal displacements consistent with the

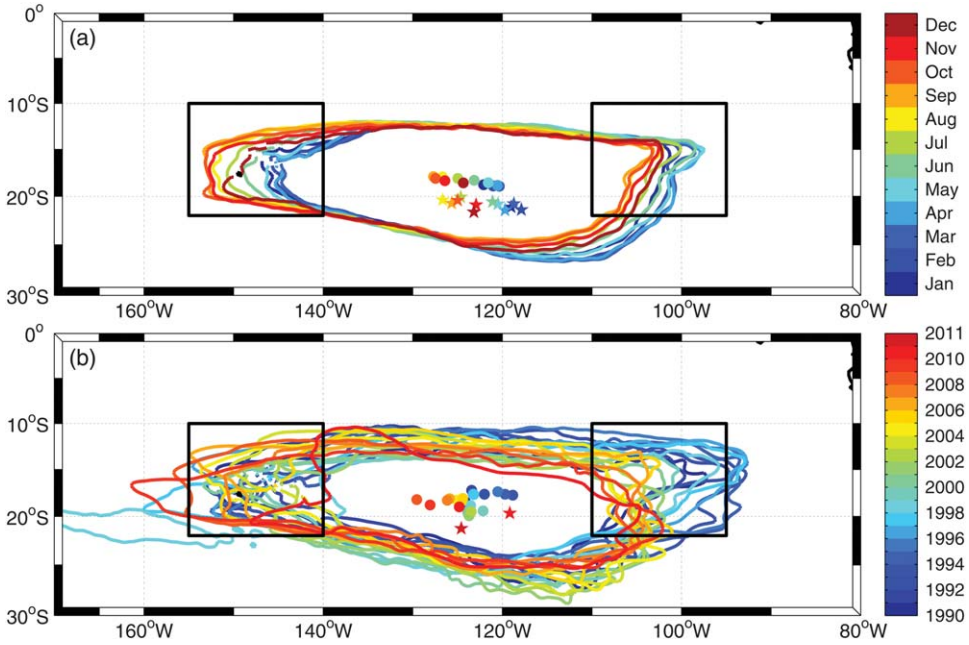

Figure 4. (a) Monthly and (b) annual mean positions of the modeled 36 isohaline. In both figures, the colored dots and stars show, respectively, the barycenter of the modeled and SMOS-derived 36 isohalines. The two rectangles denote the *east* and *west-boxes* discussed in section 4.

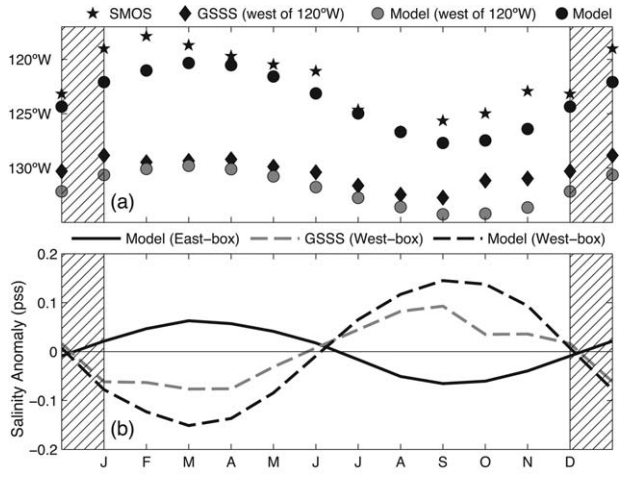

Figure 5. (a) Mean seasonal variability of the longitudinal location of the barycenter of high-salinity ($S > 36$ pss) waters based on the model (black dots) and SMOS (stars) data sets, and with data only west of 120°W for the model (gray dots) and the VOS-derived SSS gridded product (GSSS, diamond). (b) Mean seasonal SSS anomaly in the *east-box* (model—solid line) and in the *west-box* (model and gridded product—dashed lines).

one reproduced by the model, giving more confidence in the model ability to reproduce this real feature.

[18] The model offers a mean to understand the mechanisms behind this zonal cycle as each term of the MLS budget can be examined. Two zones (black boxes in Figure 4a) on the western (10°S–22°S, 155°W–140°W, *west-box*) and on the eastern (10°S–22°S, 110°W–95°W, *east-box*) sides of the high MLS core have been designed to capture its movements. Because of its displacement, the MLS variations in the two boxes are in antiphase (Figure 5b). The MLS tendency and three main processes (Figure 6) have a seasonal cycle in antiphase from east to west. The examination of each term of the MLS budget shows the prevailing role of the surface forcing in both zones, the horizontal advection and subsurface forcing being much weaker.

[19] The analysis of the surface forcing field indicates that the seasonal displacements of the high-salinity region are mainly due to the synchronous variation in the intensity and position of the SPCZ and of the Easterly winds. In austral summer (DJF), the SPCZ is very active, its eastern portion reaches the *west-box*, and *P* is high [see *Vincent*, 1994], decreasing SSS in the *west-box* (Figure 5b). The surface forcing is damped by the opposite effect of subsurface processes, which is more efficient as the surface freshening increases the vertical salinity gradient. In the *east-box*, the Easterlies are stronger than average, increasing evaporation, and SSS. Subsurface processes are less efficient since it lies in a region of subduction [*Nonaka and Sasaki*, 2007], where vertical salinity gradient across the mixed layer base is weak. From these combined effects, the high-salinity region and its barycenter reached their easternmost position in March. Following the SPCZ seasonal cycle, the reverse mechanism takes place in austral winter (JJA). The SPCZ and the associated heavy *P* move toward the equator and Easterlies are weaker than the average. As a consequence, SSS increases in the *west-box* and decreases in the *east-box*, forcing the high-salinity region and its barycenter to move back to the west.

4.2. Interannual Variability

[20] The evolution of the SSS maximum region is further investigated on time scales greater than annual, using model and observed data. Following HDD13, the low frequency signal is extracted by filtering with a 13 month Hanning filter the difference between the original time series and the mean year (except for SMOS data).

[21] The high-salinity core shows very weak variability in its barycenter meridional displacement (280 km peak-to-peak) but significant zonal displacements over the 22 year simulation (Figure 4b). The easternmost position of the mid-year (July) 36 isohaline contours shift gradually westward by about 1000 km from about 95°W in the early

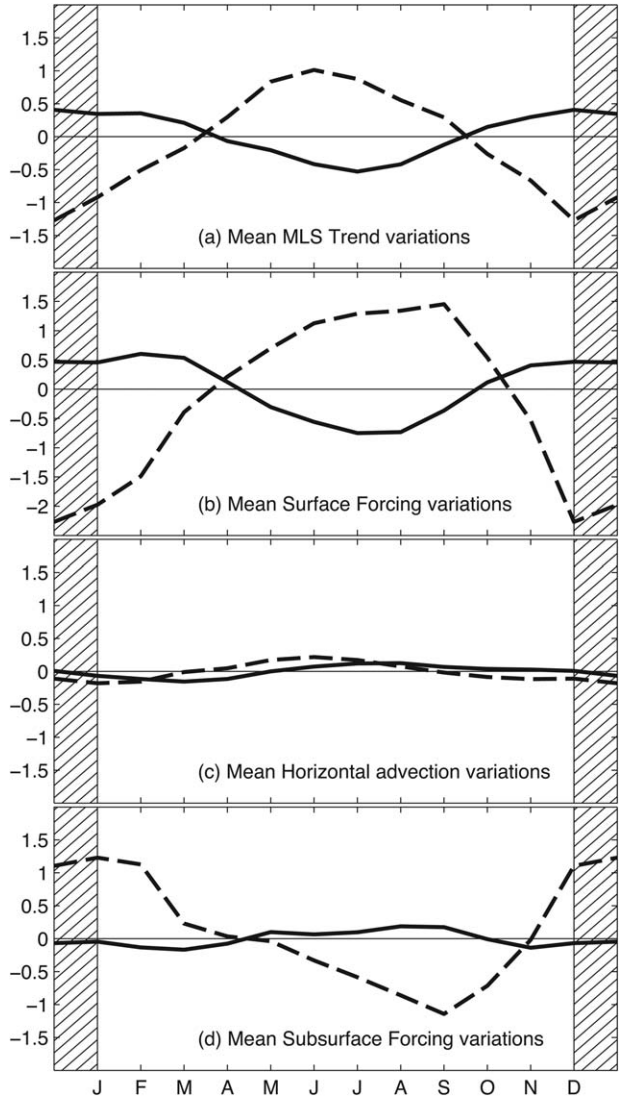

Figure 6. Mean seasonal variations of the model derived (a) MLS tendency and contributions of (b) the surface forcing, (c) the horizontal advection, and (d) the subsurface forcing within the *east* (solid lines) and *west-boxes* (dashed lines) shown in Figure 4. Units are pss/yr.

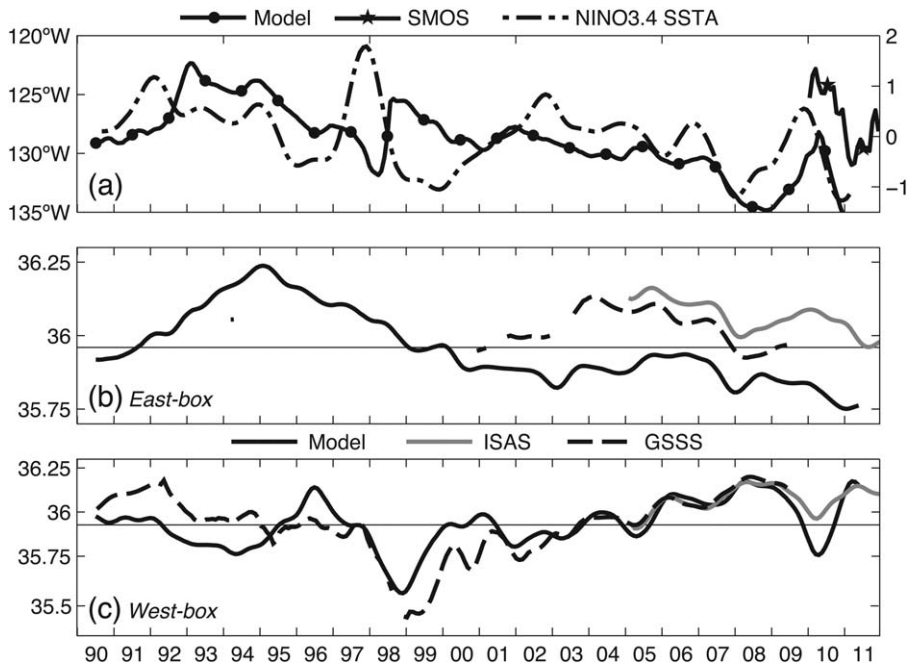

Figure 7. (a) Interannual variability of the longitudinal location of the barycenter of high-salinity ($S > 36$ pss) waters based on the model (black dots, left axis) and SMOS (stars in 2010 and 2011, left axis) data sets. Interannual sea surface temperature anomaly in the Nino3.4 region (dotted line, right axis). (b) Modeled interannual MLS (solid black line), VOS-derived SSS (dashed line), and ARGO-derived SSS (solid gray line) in the *east-box* shown in Figure 4. (c) Same as Figure 7b for the *west-box*. The horizontal thin lines in Figures 7b and 7c represent the 1990–2011 averaged modeled MLS in the *east-* and *west-boxes*, respectively. Averaged SSS from observational products are shown only when at least half of the data within the boxes is above the error criterion described in section 2.

1990s to about 105°W in the late 2000s. The position of the contours westernmost edge does not show such a steady shift during the same time period. The annual barycenter positions have an essentially zonal displacement, with a quasi-steady westward shift of the order of 1400 km during 1990–2011 (Figures 4b and 7a). Even though no certain conclusion can be drawn from the short SMOS time series, the westward shift of the barycenter does appear in 2010–2011, with a magnitude comparable to the modeled shift (stars in Figures 4b and 7a). From 2004, the region includes a sufficient number of VOS-TSG data and Argo measurements so that the two derived in situ gridded products can be compared to the model output. Despite a mean difference of the order of 5-degree of longitude with the model, both in situ data sets show a westward displacement of the barycenter location (Figure 8) in agreement with the modeled shift.

[22] Changes in modeled MLS within the *east-* and *west-boxes* are also investigated to better understand the 36 isohaline interannual zonal movement. Figures 7b and 7c indicate good agreement between the modeled MLS and the corresponding changes in observed SSS, when available. Unlike the seasonal variations, the two MLS time series are not in antiphase. The *west-box* MLS shows strong interannual variability, anticorrelated ($R = -0.6$) with a 9 month lag to the modeled NINO3.4 SST (Figure 7a) used as an ENSO index. This anticorrelation, however, mostly reflects the MLS decreases during the 1998–1999 La Nina event, in agreement with the observational results of *Gouriou and Delcroix* [2002]. The link between the *west-box* MLS variability and the remaining La Nina and El Nino events is not that clear, if any. The lack of well-marked El Nino signature is not surprizing during the Central Pacific El Niño types in 1992–1995, 2002–2005, and 2009–2010,

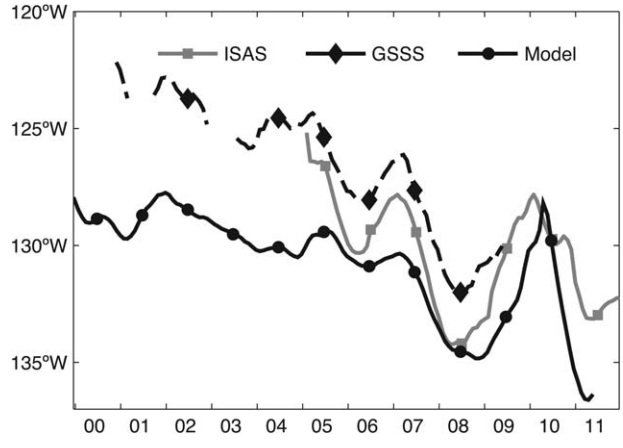

Figure 8. Interannual variability of the longitudinal location of the barycenter of high-salinity ($S > 36$ pss) waters based on the model (black dots), the VOS-derived (black diamonds) and ARGO-derived (gray squares) gridded SSS product data sets. Barycenter locations are shown for the observations only when at least half of the data within the *east-box* is above the error criterion described in section 2.

Table 1. Long-Term (1994–2011) Averaged Contribution of the Different Terms of the Mixed-Layer Salinity Budget for the So-Called *East-* and *West-Boxes* (see Figure 4)[a]

	West-Box	East-Box
Advection	−5.1	−13.5
Subsurface	+18.2	−12.7
Surface	−12.8	+ 25.9
Total	+0.3	−0.3

[a]Advection denotes the terms III + IV, subsurface the terms IV + VI, and surface the terms II in equation (1). Units are pss/18 Years.

as they were shown to have a weak regional impact on observed SSS [*Singh et al*., 2011]. In contrast, the *east-box* MLS does not exhibit interannual changes, even during 1998–1999. Figures 7b and 7c further shows that at the decadal time scale, the *west-box* MLS increases from the late 1990s to the early 2010s, whereas the *east-box* MLS freshens almost linearly from the mid-1990s to the early 2010s. This is consistent with the quasi-linear westward shift of the 36-isohaline barycenter position. Except when we have sufficient observations, conclusions should be drawn with care. One should keep in mind that such a westward shift cannot be checked over two complete decades with observations in the eastern half of the high-salinity core.

[23] All terms of the MLS budget in the eastern and western boxes were also investigated in order to understand mechanisms responsible for the low-frequency displacement of the high-salinity core. In agreement with the analysis above, all terms are found to be statistically uncorrelated to the modeled NINO3.4 SST (or other ENSO indices), preventing us to derive conclusions regarding possible ENSO effects. At the decadal time scale, Table 1 indicates that the long-term mean salinity tendency over 1994–2011 is about +0.3 and −0.3 in the *west* and *east-boxes*, respectively. These MLS changes reflect the contribution of the surface forcing, subsurface forcing, and horizontal advection terms, which are mostly of analogous importance, nearly compensating each other. They are also 1 order of magnitude larger than the resulting MLS tendency. As a consequence, it is difficult to identify the true origin(s) of the modeled westward shift (that does exist in nature), which is mainly due to a small decrease of the *east-box* salinity and to a small increase of the *west-box* salinity. Both salinity changes are small residual of large changes in the corresponding MLS terms.

5. Summary and Conclusions

[24] This study examines causes for the formation and variability of the salinity maximum waters (SSS > 36) located in the south-eastern tropical Pacific (centered at 18.4°S and 123.8°W) and covering a region of about 5.2×10^6 km^2 over the 1990–2011 period. This work relies on in situ and SMOS-derived SSS data to document the main features and on a validated DRAKKAR simulation to quantify mechanisms at play. This work is motivated by the need to improve our understanding of maximum salinity waters, in line with the interpretation of climate and hydrological cycle changes at different time scales.

[25] From the model output, waters with salinity above 36 pss result from a balance between the surface forcing ($E-P$) that increases the MLS by about 0.73 pss/yr, and the compensating horizontal advection and subsurface forcing. Each of these two processes decreases the salinity by about half of the surface forcing. The ratio between the three processes is consistent with what was found by *Qu et al*. [2011] in the North Atlantic Salinity Maximum. The modeled salinity maximum waters have their 20 year average salinity increasing by 0.02 pss/yr which is qualitatively consistent with the "dry get dryer" paradigm although stronger than the estimated from different observation data sets and time periods by *Terray et al*. [2012] and *Durack and Wijffels* [2010]. The observations and the models both show high-salinity waters variability at the seasonal and longer time scales. At the seasonal time scale, salinity maximum waters shift eastward in austral summer and westward in austral winter, with an amplitude of 400 km. This is the consequence of the changing intensity of the SPCZ and Easterly winds that modulate P and E, respectively. At longer time scales, the salinity maximum waters barycenter was found to move westward by about 1400 km during mid 1990 to early 2011, with no clear relationship with the occurrence of individual El Nino/La Nina events.

[26] While we have assessed processes responsible for the formation and seasonal variability of the maximum salinity waters, using different types of data, we have not clearly identified causes for the low-frequency variability. The westward shift of the salinity maximum waters remains puzzling, and is worth to be further investigated. The shift is not noticeably linked to ENSO, though it corresponds to a tendency for more La Nina than El Nino events (see the cooling trend of NINO3.4 SST in Figure 7a). It also corresponds to a tendency for more Central than Eastern Pacific El Nino types during 1990–2011, suggesting a plausible association with ENSO. Interestingly, our findings are consistent with the expected effects of the westward shift of the eastern edge of the SPCZ (and related regional P decrease) in future climate projections [*Brown et al*., 2012]. It however somewhat differs from the poleward (and not westward) shift of the south-eastern Pacific dry zone and southwestward extension of the high-salinity waters predicted by general circulation models in a warming world [*Seager et al*., 2010; *Scheff and Frierson*, 2012; *Ganachaud et al*., 2012]. The question about the westward shift is likewise of interest for biological studies, bearing in mind that salinity maximum waters in the studied region partly overlap with oligotrophic waters that have been shown to expand both northward and southward in recent years [*Polovina et al*., 2008]. Also, the impact of changes in the location of the high SSS core could impact the STC as noted in section 1. It is clearly another interesting issue through its potential impact on the downstream salinity fields, and possibly the mean background state of the equatorial band.

[27] The degree of confidence we can have in the model outputs and/or its ERA-interim forcing sets from which we derived part of our results is obviously a central question. The DRAKKAR model basic variables have been carefully validated in earlier studies [e.g., *Barnier et al*., 2006; *Hasson et al*., 2013]. In particular, it was shown that the model captures well the observed mean, seasonal, and interannual SSS changes of the tropical Pacific.

Furthermore, it provided a good representation of the observed surface zonal currents obtained from the TAO-TRITON moorings at 110°W, 140°W, 165°E, and 156°E (i.e., the only long time series of direct current observations). The model outputs (and/or its ERA-interim forcing sets) are, however, obviously not perfect. We know, for instance, that the modeled equatorial zonal current variability tends to be underestimated by about 75%, and that the modeled MLD is on average 21% shallower than the observed MLD [*Hasson et al*., 2013]. The roles of such biases on the present results are not clear and admittedly need to be examined in details in further studies. Moreover, *Hasson et al*. [2013] have shown the present difficulty, not to say impossibility, to rigorously evaluate terms involved in the MLS balance using low-resolution gridded observational data only, such as gridded SSS products and surface currents estimated from altimetry and Ekman drifts. In other words, we cannot be 100% sure that the model reproduces the observed features for the good reasons. Notwithstanding, when observations are available, the systematic good correspondence between the observed and modeled mean and variability of the South Pacific SSS maximum indicates the likeliness of our results to be realistic. Based on about two decades of data only, it would be of great interest to extend our investigation with longer MLS time series, such as future in situ and remotely sensed observations, other validated model simulations, and/or climate model projections.

[28] **Acknowledgments.** This work is a contribution to the ESA GLOSCAL SMOS project. It is supported by CNES/TOSCA SMOS-Ocean and by ESA SMOS + SOS projects. We benefited from numerous data sets made freely available, including those from the French SSS Observation Service and from the DRAKKAR model group. The LOCEAN_v2013 Sea Surface Salinity maps have been produced by LOCEAN/IPSL laboratory that participates to the Ocean Salinity Expertise Center (CECOS) of Centre Aval de Traitement des Donnees SMOS (CATDS). Discussions with G. Alory from LEGOS in Toulouse, the programming support of N. Martin and O. Hernandez from LOCEAN in Paris regarding the SMOS data and R. Dussin from LEGI in Grenoble regarding the model simulation and comments from anonymous reviewers were deeply appreciated.

References

Barnier, B., et al. (2006), Impact of partial steps and momentum advection schemes in a global ocean circulation model at eddy-permitting resolution, *Ocean Dyn.*, *56*(5–6), 543–567, doi:10.1007/s10236-006-0082-1.

Boutin, J., N. Martin, G. Reverdin, X. Yin, and F. Gaillard (2013), Sea surface freshening inferred from SMOS and ARGO salinity: Impact of rain, *Ocean Sci.*, *9*, 183–192, doi:10.5194/os-9–183-2013.

Brown, J., A. Moise, and R. Colman (2012), The South Pacific Convergence Zone in CMIP5 simulations of historical and future climate, *Clim. Dyn.*, *1–19*, doi:10.1007/s00382-012-1591-x.

Cravatte, S., T. Delcroix, D. Zhang, M. McPhaden, and J. Leloup (2009), Observed freshening and warming of the western Pacific Warm Pool, *Clim. Dyn.*, *33*(4), 565–589, doi:10.1007/s00382-009-0526-7.

Delcroix, T., and C. Henin (1991), Seasonal and interannual variations of sea surface salinity in the Tropical Pacific Ocean, *J. Geophys. Res.*, *96*(C12), 22,135–22,150.

Delcroix, T., G. Alory, S. Cravatte, T. Correge, and M. J. McPhaden (2011), A gridded sea surface salinity data set for the tropical Pacific with sample applications (1950–2008), *Deep Sea Res., Part I*, *58*(1), 38–48, doi:10.1016/j.dsr.2010.11.002.

Durack, P. J., and S. E. Wijffels (2010), Fifty-year trends in global ocean salinities and their relationship to broad-scale warming, *J. Clim.*, *23*(16), 4342–4362, doi:10.1175/2010jcli3377.1.

Foltz, G. R., and M. J. McPhaden (2008), Seasonal mixed layer salinity balance of the tropical North Atlantic Ocean, *J. Geophys. Res. Oceans*, *113*, 1-14, doi:10.1029/2007JC004178.

Gaillard F., E. Autret, V. Thierry, P. Galaup, C. Coatanoan, and T. Loubrieu, (2009), Quality Control of Large Argo Datasets, *J. Atmos. Ocean. Technol.*, *26*(2), 337–351, doi: 10.1175/2008jtecho552.1.

Ganachaud, A., A. Sen Gupta, J. N. Brown, K. Evans, C. Maes, L. C. Muir, and F. S. Graham (2012), Projected changes in the tropical Pacific Ocean of importance to tuna fisheries, *Clim. Change*, *1–17*, doi:10.1007/s10584-012-0631-1.

Gouriou, Y., and T. Delcroix (2002), Seasonal and ENSO variations of sea surface salinity and temperature in the South Pacific Convergence Zone during 1976–2000, *J. Geophys. Res. Oceans*, *107*(C12), 8011, doi: 10.1029/2001JC000830.

Gu, D. F., and S. G. H. Philander (1997), Interdecadal climate fluctuations that depend on exchanges between the tropics and extratropics, *Science*, *275*(5301), 805–807, doi:10.1126/science.275.5301.805.

Hasson, A. E. A., T. Delcroix, and R. Dussin (2013), An assessment of the mixed layer salinity budget in the tropical Pacific Ocean. Observations and modelling (1990–2009), *Ocean Dyn*., *63*(2–3), 179–194, doi: 10.1007/s10236-013-0596-2.

Held, I. M., and B. J. Soden (2006), Robust responses of the hydrological cycle to global warming, *J. Clim.*, *19*(21), 5686–5699, doi:10.1175/jcli3990.1.

Henin, C., and J. Grelet (1996), A merchant ship thermo-salinograph network in the Pacific Ocean, *Deep Sea Res., Part I*, *43*(11–12), 1833–1855, doi:10.1016/s0967-0637(96)00084-2.

Kolodziejczyk, N., and F. Gaillard (2012), Observation of spiciness interannual variability in the Pacific pycnocline, *J. Geophys. Res.*, *117*, C12018, doi:10.1029/2012JC008365.

Laurian, A., A. Lazar, and G. Reverdin (2009), Generation mechanism of spiciness anomalies: An OGCM analysis in the North Atlantic subtropical gyre, *J. Phys. Oceanogr.*, *39*(4), 1003–1018, doi:10.1175/2008jpo3896.1.

Levitus, S. (1986), Annual cycle of salinity and salt storage in the World Ocean, *J. Phys. Oceanogr.*, *16*(2), 322–343, doi:10.1175/1520-0485(1986)016<0322:acosas>2.0.co;2.

Madec, G. (2008), *NEMO Ocean Engine*, p. 300, Inst. Pierre-Simon Laplace, Paris, France.

McCreary, J. P., and P. Lu (1994), Interaction between the Subtropical and Equatorial Ocean Circulations—The subtropical cell, *J. Phys. Oceanogr.*, *24*(2), 466–497.

McPhaden, M. J., and D. X. Zhang (2004), Pacific Ocean circulation rebounds, *Geophys. Res. Lett.*, *31*, 1–19, doi:10.1029/2004GL020727.

Nonaka, M., and H. Sasaki (2007), Formation mechanism for isopycnal temperature-salinity anomalies propagating from the eastern South Pacific to the equatorial region, *J. Clim.*, *20*(7), 1305–1315, doi:10.1175/jcli4065.1.

O'Connor, B. M., R. A. Fine, K. A. Maillet, and D. B. Olson (2002), Formation rates of subtropical underwater in the Pacific Ocean, *Deep Sea Res., Part I*, *49*(9), 1571–1590, doi:10.1016/s0967-0637(02)00087-0.

Polovina, J. J., E. A. Howell, and M. Abecassis (2008), Ocean's least productive waters are expanding, *Geophys. Res. Lett.*, *35*, 1–4, doi:10.1029/2007GL031745.

Qu, T., S. Gao, and I. Fukumori (2011), What governs the North Atlantic salinity maximum in a global GCM?, *Geophys. Res. Lett.*, *38*, 1–6, doi:10.1029/2011GL046757.

Reul, N., et al. (2013), Sea surface salinity observations from space with the SMOS satellite: A new means to monitor the Marine branch of the water cycle, *Surv. Geophys.*, *1–42*, doi:10.1007/s10712-013-9244-0.

Scheff, J., and D. M. W. Frierson (2012), Robust future precipitation declines in CMIP5 largely reflect the poleward expansion of model subtropical dry zones, *Geophys. Res. Lett.*, *39*, 1–4, doi:10.1029/2012GL052910.

Schneider, N., A. J. Miller, M. A. Alexander, and C. Deser (1999), Subduction of decadal North Pacific temperature anomalies: Observations and dynamics, *J. Phys. Oceanogr.*, *29*(5), 1056–1070, doi:10.1175/1520-0485(1999)029<1056:sodnpt>2.0.co;2.

Seager, R., N. Naik, and G. A. Vecchi (2010), Thermodynamic and dynamic mechanisms for large-scale changes in the hydrological cycle in response to global warming, *J. Clim.*, *23*(17), 4651–4668, doi:10.1175/2010jcli3655.1.

Singh, A., T. Delcroix, and S. Cravatte (2011), Contrasting the flavors of El Nino-Southern Oscillation using sea surface salinity observations, *J. Geophys. Res.*, *116*, C06016, doi:10.1029/2010JC006862.

Terray, L., L. Corre, S. Cravatte, T. Delcroix, G. Reverdin, and A. Ribes (2012), Near-surface salinity as nature's rain gauge to detect human influence on the tropical water cycle, *J. Clim.*, *25*(3), 958–977, doi: 10.1175/jcli-d-10–05025.1.

Vincent D. G., (1994), The South Pacific Convergence Zone (SPCZ) — A Review, *Mon. Weather Rev.*, *122*(9), 1949–1970, doi:10.1175/1520-0493(1994)122<1949:tspcza>2.0.co;2.